A thin elastic plate model for thermally contracting young oceanic lithosphere: Insights from comparison with modern seafloor observations

Eunseo Choi[1] and Masako Tominaga[2]

[1]Center for Earthquake Research and Information, the University of Memphis, 3890 Central Ave., Memphis, TN 38152, USA

[2]Dept. Geology and Geophysics, Woods Hole Oceanographic Institution

Abstract

We find at fast- and intermediate-spreading seafloor that their ridge-parallel bathymetric profiles between two neighboring fracture zones, excluding the part of the seafloor inward to fracture zone valley, are predominantly upward concave. The temporal evolution of the bathymetric profiles from the lithosphere formed at the Chile Rise is characterized by (i) the rapid growth of the middle deflection to about 200 m relative to the ends for the first few millions of years and (ii) a steady state afterwards. We show that these characteristics and the upward-concave sense of bending can be reasonably explained as the flexure of a thin elastic plate contracting thermally from the top while cooling. The best-fitting model needs only about 10 % of the thermal bending moment based on the half-space cooling model and the free-end assumption. Our model is consistent with the recent observations that oceanic lithosphere is cut open at a fracture zone valley, which disprove the previous assumption that ocean floor is bent down forming the valley walls.

Plain Language Summary

Plate tectonics is one of the most prominent planetary activities that characterize the Earth. To fully understand the nature and behavior of plates that shape the Earth's surface, it is important to closely examine physics of these plates. We focus on one of the effects of volume change that an oceanic plate experiences as it cools down since formed at mid-ocean ridges. We analyzed bathymetric profiles taken parallel to mid-ocean ridges at several locations around the world including the Chile Rise in the Pacific Ocean. We found them upward-concave with about 200 m height difference between the middle and the ends of the profiles. Adopting a thin elastic plate model, we show that the observed characteristics of the bathymetric profiles can be explained as thermal contraction of a thin elastic plate cooling from the top. Our study confirms the importance of understanding how the volume change of oceanic lithosphere occurs.

Key Points:

1. The ridge-parallel bathymetric profiles of oceanic lithosphere between fracture zones are upward concave.
2. The upward-concave profiles can be explained as the bending of a thin elastic plate cooling and contracting from the top.
3. Our thermal contraction model is consistent with the recent observations that oceanic lithosphere is cut open at a fracture zone valley.

1. Introduction and Background

Understanding properties that control kinematics of oceanic lithosphere is essential in addressing geodynamics in global tectonics, such as subduction and rift initiation, plate boundary reconfiguration, and intraplate volcanism (e.g., Forsyth, 1979; McNutt, 1984; Sandwell, 1986). While many studies treated the behavior of oceanic lithosphere in response to the stress field with the rigid-plate assumption (Wilson, 1965), the evolution of uppermost oceanic lithosphere, namely the brittle, ocean crust, cannot be described solely with such assumption. Oceanic lithosphere's first order characteristics including age-dependent bathymetry originates from thermal contraction and densification occurring as lithosphere cools over time (Buck, 2001; Haxby & Parmentier, 1988; Kumar & Gordon, 2009; Mishra & Gordon, 2016; D. Sandwell & Fialko, 2004; D. Sandwell & Schubert, 1982; Wessel, 1992; Wessel & Haxby, 1990). With a typical rock's volumetric thermal expansion coefficient of 3×10^{-5} K^{-1}, a temperature decrease of 500 K can cause 1.5 % of volume reduction. If we simply apply one third of it to 0.5 % of length change in one dimension, then this translates into the displacement of 5 km over a 1000 km-long crustal block with seawater. Such amounts of strain should be associated with observable deformations. When the thermal contraction cannot occur freely, thermal stress arises. With crustal rocks' elastic moduli on the order of 10^{11} Pa, a strain of 0.5 % means a stress magnitude on the order of 100s of MPa, which is sufficient for causing brittle deformation in upper oceanic lithosphere (Choi & Gurnis, 2008). For this reason, thermal contraction and associated stress in oceanic lithosphere also has important implication for hydration of oceanic lithosphere through hydrothermal circulation into the deeper portion of lithosphere, a ubiquitous process operating from mid-ocean ridges to convergent margins (Kohli & Warren, 2020; Prigent et al., 2020).

Thermal contraction of oceanic lithosphere was invoked for explaining bathymetry data from global seafloor mapping effort unfolded in 1980s'. For instance, Parmentier and Haxby (1986, hereafter PH86) modeled the observed bathymetric profiles on the lithosphere sectored between oceanic fracture zones using a thin elastic plate model. Their decision to include the fracture zone valleys in the bathymetric profiles to be modeled (Fig. 1A) led to the thin elastic plate model with both ends bending downwards (Fig. 1A). The model implies that the internal layers of the oceanic lithosphere would conform to the fracture zone valley walls (Fig. 1A) rather than be crosscut by them.

However, as more *in situ* observations and higher resolution global seafloor data have become available over the last few decades, further deviation between our understanding of oceanic lithosphere and the implications of PH86 model grew. The deviation would soon become non-negligible as our knowledge has recently been advanced about much higher resolution on interplay between tectonics and magmatism that characterizes fracture zone valley and the behavior of adjacent oceanic lithosphere than a few decades ago when the PH86 model was proposed (e.g. Wang et al., 2022; Gregory et al., 2021; Grevemeyer et al., 2021; Kohli et al., 2021). With a simple view, the deviation can be described in a few key points. First, where the inner walls of a fracture zone expose a section of oceanic lithosphere, the inner wall lithology implies the "transverse ridge" along a fracture zone is a product of upward bending (Bonatti et al., 2005; Cannat et al., 1991; Gregory et al., 2021; Juteau et al., 1995; Marjanović et al., 2020; Ren et al., 2022). Then, seafloor observations reveal that geological processes about flexure evolution from axis to off-axis following the flowline of a spreading corridor is seemingly more complicated as (i) not only both sides of fracture zones are off-set of lithosphere/depths – one or both sides can be characterized by ridges and other tectonic inheritances from spreading-rates dependent mid-ocean ridge axes; and (ii) incipient propagators, globally observed near-axes and off-axis seamount chains and volcanic addition make the topography of lithosphere sectored by fracture

zones elevated from adjacent seafloor. With improved resolution of seafloor bathymetry since PH86, e.g. the effort of multi-scale bathymetry compilation (Ryan et al., 2009) and new satellite altimetry-based global coverage (Sandwell et al., 2014), and advanced knowledge on the seafloor observations today, we revisit thermal contraction within young oceanic lithosphere, which is intrinsically related to the origin and nature of flexure, using such modern data.

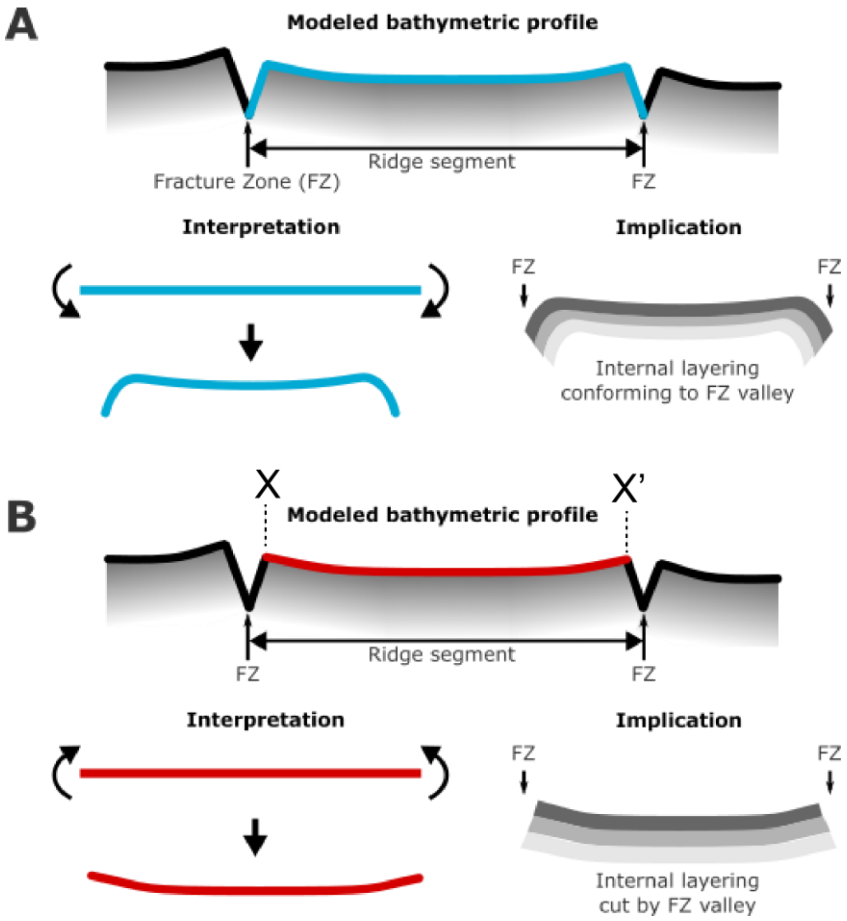

Figure 1. A schematic explanation on two models for lithosphere flexure due to thermal contraction. (A) The model including the fracture zone valley (e.g., Parmentier and Haxby, 1986). The sense of bending is consistent with "growing plate" cooling model (e.g. Wessel, 1992). (B) The model from this study that excludes fracture zone valleys. The senses of bending moment are opposite to (A). Model A implies internal layering conforming to the fracture zone valleys while model B is consistent with the internal layering cut and exposed by them. The sense of bending is consistent with "static plate" cooling model (this study).

In this study, we start with presenting the evolution of seafloor topography between transform faults over 20 Ma using a publicly accessible ETOPO 1-arc minute global bathymetry compilation with satellite altimetry data (Fig. 2). We then calculate the flexure of an elastic thin plate driven by bending moment based on the half-space cooling model. The point of departure from the PH86 model is that we exclude fracture zone walls from the bathymetric profiles to be modeled (Fig. 1B), motivated by the observed cross sections of oceanic lithosphere exposed on the fracture zone walls described above. We show that our thin elastic plate model well captures the main characteristics of bathymetric

evolution within a case study area, the Chile Rise oceanic lithosphere, despite limitations stemming from the simplifying assumptions we made.

2. Methods

2.1 Seafloor observations

As being inspired by the approach PH86 had taken in assessing their model (e.g. Fig.4 in Parmentier & Haxby, 1986), we made a first-order assessment on the maturation/evolution of oceanic lithosphere along the age flow line between two neighboring fracture zones. Although "long-lived" fracture zones are ubiquitous in the world's ocean, there are only a few that are suitable to use as a basis for our modeling. The lithosphere we should focus on are: (1) fast-to-intermediate spreading lithosphere bounded by two continuous transform faults/fracture zones observed within the ETOPO bathymetry compilation grids; (2) crustal ages and spreading rates (i.e. fast- ~ 74 mm/yr half rate and intermediate 28-34 mm/yr half rate, e.g. Buck et al., 2005) were determined by unambiguous interpretation of observed marine magnetic anomalies in previously published literatures; and (3) the extent of the ridge to off-axis reaches up to 20 Myr in age and is as little tectonically and volcanically disturbed/overprinted as possible. Many of these lithosphere segments include propagator wakes (particularly pronounced in the Mid-Atlantic Ridge (MAR) segments and their transform faults in the South Atlantic), and volcanic ridges and seamounts, being found unideal to capture our numerical model parameterization and results. Consequently, there is a very limited number of seafloor segments available for our study.

With considering above criteria, after examining various portions of globally well-documented, fast-intermediate spreading segments (see Figs. S1 and S2 as a set of examples), we here present a representative portion of lithosphere that has been evolved at the western flank of intermediate spreading Chile Rise (60 mm/yr full rate) in between Valdivia and Guano fracture zones (Tebbens & Cande, 1997a) (Fig.2). With ETOPObathymetry (Figs. 2a and c), we also use 1-arc minute global gravity grids (Sandwell et al., 2014) (Figs. 2b and d) to examine possible presence of major tectonic structures hidden by thick sediment cover. In addition to Chile Rise, both east and west flanks of fast spreading East Pacific Rise 9N (110 mm/yr full rate) and eastern flank of the Udintsev fracture zone (FZ) (76 mm/yr full rate, and the profiles examined in PH86) are assessed for reference (Figs. S1 and S2). To confirm the segments are mostly free of major structural overprint, we have examined vertical gravity gradient data as our check point (e.g., Sandwell et al., 2014) as well.

Ridge-parallel profiles (X-X' in Fig.1) were extracted in between the edge of the lithosphere dissected by Valdivia and Guano fracture zones (Figs. 2c and d). Ridge-parallel profiles of depth and free-air gravity anomaly were obtained with 0.2 km data sampling frequency along the profile and with 2km spacing along the spreading flow-line from the 0 (ridge) to ~ 20 Ma age crust estimated from their spreading rate (Tebbens & Cande, 1997b). To extract representative profiles of the bathymetry and gravity data to compare with numerical results, we: (i) group the sampled depth and gravity profiles into the five time periods, 0-3, 3-6, 6-10, 10-15 and 15-20 Ma; (ii) smoothed each profile by convolving it with a linear kernel (Text S1); and (iii) fitted the smoothed profiles to a polynomial (Fig. S3 and S4). We did not explicitly consider the effects of sediments (see Text S2).

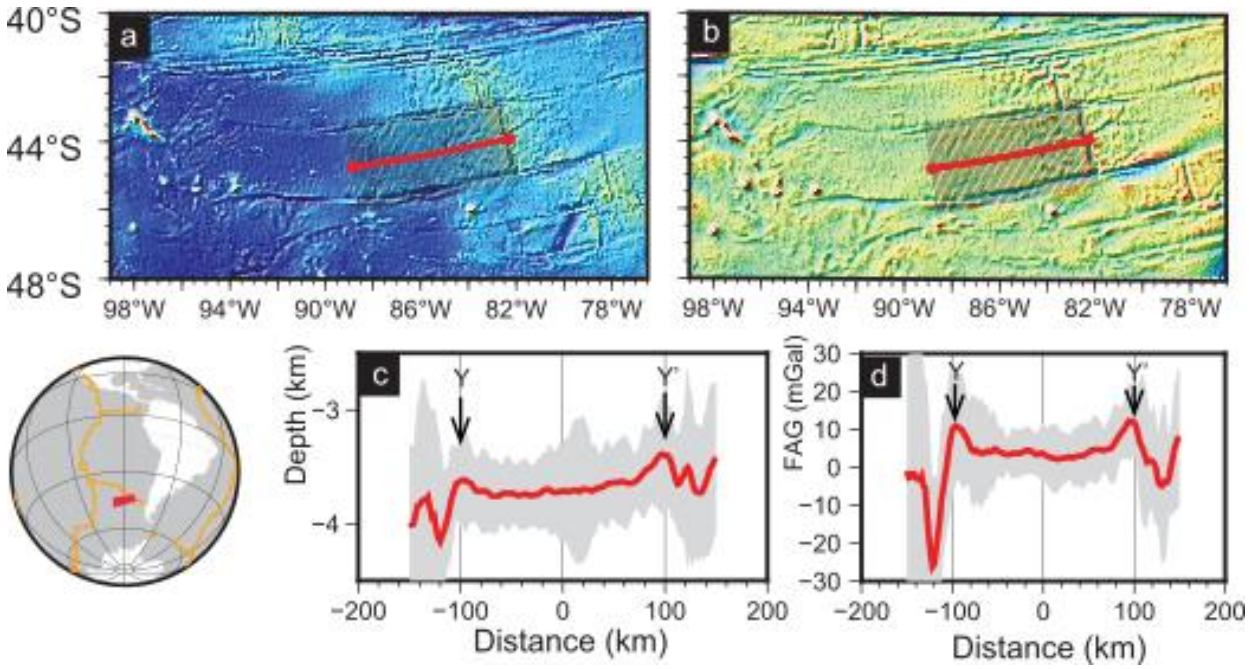

Figure 2. A summary of bathymetry profiles taken from Chile Rise (red marked region in the inset globe). (a): ETOPO-1 1-arc minute seafloor topography map including a series of transform faults formed by southern East Pacific Rise. (b): Global satellite gravity grid (v23.1, Sandwellet al., 2014). Extracted bathymetry (c) and gravity (d) profiles in gray shaded areas along ridge-parallel solid black lines in (a) and (b), respectively, with the underlying red lines showing 0-20 Myr age flow lines of this spreading corridor. Red curves in (c) and (d) show arithmetic mean of all the extracted curves. Y-Y' corresponds with the model X-X' in Fig.1. Images shown are produced by GMT v.6 (Wessel et al., 2019).

2.2 Application of thin elastic plate model

Toward building our new model, we adopt a few simplifying assumptions for approximating lithosphere as a thin elastic plate that were made first in PH86 and then used in subsequent studies (e.g., Haxby & Parmentier, 1988; Parmentier & Haxby, 1986; Wessel, 1992; Wessel & Haxby, 1990). Firstly, newly-formed oceanic lithosphere is assumed to freely contract in the ridge-parallel direction (x) as it cools down. Secondly, the cooling and freely-contracting lithosphere can still bend in a consistent way with the deviatoric strain, $\epsilon_{xx} - \overline{\epsilon}_{xx}$, where $\overline{\epsilon}_{xx}$ is the depth average of ϵ_{xx}. If bending is prohibited due to kinematic constraints on the lithosphere, the corresponding bending stress would arise. Thirdly, the lithosphere is assumed to be elastic when its temperature (T) is at or lower than a brittle-ductile transition temperature, T_l. Thermal stress, if any, would dissipate completely and sufficiently fast by viscous relaxation when $T > T_l$. Finally, depth-dependent of temperature within the elastic portion of lithosphere is assumed to be linear, an approximation well-justified in the light of the half-space or a plate cooling model. With elastic thickness at time t denoted as h(t), the depth (z) distribution of temperature within the elastic portion is given as $T(z, t) = T_l\, z / h(t)$.

The above assumptions yield an expression for ridge-parallel thermal strain $\epsilon_{xx}(z,\ t)$:

$$\epsilon_{xx}(z,t) = \alpha_l\,(T(z) - T_l) = \alpha_l\, T_l \left(\frac{z}{h(t)} - 1\right), \tag{1}$$

where α_l is the linear thermal expansion coefficient. This expression holds for $0 \leq z \leq h(t)$ for any $h(t)$ and ϵ_{xx} is zero or negative (i.e., contractional) for all depths, $0 \leq z \leq h(t)$. The mean horizontal strain, $\overline{\epsilon}_{xx}$, is defined as

$$\overline{\epsilon}_{xx}(t) = \int_0^{h(t)} \epsilon_{xx}(z) dz / h(t).$$

For the linear top-down cooling considered here, $\overline{\epsilon}_{xx}$ becomes a constant,

$$\overline{\epsilon}_{xx} = -\frac{1}{2}\alpha_l T_l \,. \tag{2}$$

Then, we get deviatoric horizontal strain, ϵ'_{xx} from eqs. (1) and (2):

$$\epsilon'_{xx}(z,t) = \epsilon_{xx}(z,t) - \overline{\epsilon}_{xx} = \alpha_l T_l \left(\frac{z}{h(t)} - \frac{1}{2}\right). \tag{3}$$

The bending moment (*M*) required for a flat, stress-free, thin elastic plate to generate the flexure compatible with the deviatoric thermal strain given by eq. (3) can be expressed in terms of the deviatoric stress, σ'_{xx}:

$$M(t) = \int_0^h \sigma'_{xx}(z,t)\, z \,\mathrm{d}z = E' \int_0^h \epsilon'_{xx}(z,t)\, z \,\mathrm{d}z, \tag{4}$$

where E' is $E/(1-\nu)$ and E and ν are the Young's modulus and the Poisson's ratio (Turcotte and Schubert, 2014). From (3) and (4), we get the following expression:

$$M(t) = \alpha_l E' T_l \int_0^{h(t)} \left(\frac{z}{h(t)} - \frac{1}{2}\right) z \,\mathrm{d}z = \frac{1}{12}\alpha_l E' T_l h(t)^2. \tag{5}$$

The moment in eq. (5) generates upward-concave bending of the plate (Fig. 1B). Upward concavity is the sense of bending expected for the "static plate" cooling from the top. The "static plate" model is one of the end-member models for how thermal strain accumulates in oceanic lithosphere over time while cooling (e.g., PH86; Wessel, 1992). Another end-member is the "growing plate" cooling model (Wessel, 1992), in which the brittle portion is assumed to have contracted freely before a new layer that has just become brittle is added at the bottom and starts contracting. The sense of bending in the growing plate model is depicted in Fig. 1A. Although the way thermal strain actually accumulates in cooling oceanic lithosphere must fall between these end-member modes, we adopt the "static plate" model in this study because it is consistent with the sense of bending seen in the bathymetric profiles (Fig. 2).

The equation for a thin elastic plate with the isostatic restoring force and without any horizontal boundary force is

$$w(x,t)'''' + \frac{(\rho_m - \rho_w)g}{D(t)} w(x,t) = 0, \tag{6}$$

where $D(t)$ is the flexural rigidity, $Eh(t)^3/\left(12(1-\nu^2)\right)$ (e.g., Turcotte & Schubert, 2014; Watts, 2001), ρ_m and ρ_w are the mantle and water densities, and g is the gravitational acceleration.

The bending moment given by eq. (5) is an overestimation because the deviatoric thermal contraction cannot occur freely in oceanic lithosphere because of the water pressure and the resistance to bending at the fracture zone boundaries. Thus, we introduce effective bending moment and flexural rigidity, $M_e(t)$ and $D_e(t)$, using them for solving eq. (6). With a misfit defined as $\|w_\mathrm{obs} - w\|/\|w_{obs}\|$

with $\|v\|$ being the Euclidean norm of a vector v, the optimal values of $M_e(t)$ and $D_e(t)$ are those that minimizes the sum of the misfits of the Chile Rise profiles for the five time periods; and they are $0.09M(t)$ and $0.9D(t)$, respectively (Text S3). The coefficients, 0.09 and 0.9 are constant and the cooling effects is introduced through $M(t)$ and $D(t)$.

We apply the boundary conditions for the pinned ends: $w(0,t) = 0$ and $w''(0,t) = M_e(\mathrm{t})/D_e(t)$ on the left (i.e., $x = 0$); and $w(L) = 0$ and $w''(L,t) = M_e(\mathrm{t})/D_e(t)$ on the right (i.e., $x = L$) end, where L is the length of the elastic plate. The details of acquiring approximate solutions to (6) under these boundary conditions are provided in Supplementary Information (Text S4). Another possible set of boundary conditions is to set w''' instead of w to be zero. The qualitative characteristics of the modeled flexure are retained with either choice of boundary conditions.

In summary, the best-fitting deflections are those of a 200 km-long thin elastic plate with pinned ends for T_l=500°C, ν = 0.25, E=100 GPa, ρ_{m} = 3300 kg/m^3, ρ_{w} =1030 kg/m^3, g = 9.8 m/s^2, $M_e(t)$ = $0.09M(t)$ and $D_e(t)$ = $0.9D(t)$. The modeled deflection profiles are averaged over each of the time intervals used for the bathymetric profiles (see Sec. 2.1). To facilitate the comparison of the thin plate deflections with the bathymetric profiles, we vertically adjusted the bathymetric profiles such that their left-end depth becomes to 0 m (Fig.3).

3. Results

Ridge-parallel bathymetry profiles from the fracture-zones bounded lithosphere formed at Chile Rise show temporal changes in their concavity for crustal ages less than 10 Ma and then an apparently steady state over time older than the 10 Ma crustal age. To best capture the first-order lithosphere curvature evolution over time, we have divided timeseries of lithosphere evolution to 0-3, 3-6, 6-10, 10-15, and 15-20 Ma spans of crustal age group (Fig. 3). During the first 0-3 Ma, we observe slight upward "bulge" in the middle of the averaged profile, seemingly superposed on a broadly upward-concave profile (Fig. 3a). The older (3-6 and 6-10 Ma) age seafloor exhibits reduced magnitude of the middle bulge (Fig. 3c, e). The middle part becomes about 200 to 220 m deeper than the ends. The 10 Ma or older seafloor shows upward concave profiles without visible perturbations. The depth difference between the middle and the ends of the profiles stays near 200 m (Fig.3g, i and Figs. S2). The averaged and smoothed profiles of free air gravity anomaly (FAA) also show clear upward concavity with the difference between maximum and minimum (ΔFAA) of 10-15 mGal for the first 10 Ma (Fig. 3b, d, f). The upward concavity is discernible but less pronounced in the gravity anomaly profiles for later time periods (Fig. 3h, j) with the end-to-center difference decreasing to 5-10 mGal.

The maximum downward deflection of the best-fitting thin elastic plate is about 120 m in the 0-3 Ma profile (Fig.3a) but increases to about 240 m in the next 3 Ma interval (Fig.3c). The deflection profile barely changes for the following 4 Ma (Fig. 3e) but after 10 Ma, the downward deflection decreases to about 200 m in the 10 to 15 Ma interval (Fig. 3g), and to 180 m in the 15-20 Ma (Fig. 3i). The origin of the relatively large misfits of 0.2 to 0.4 (defined in Sec. 2.2) for the first three time periods is a middle bulge seen in Fig. 3a and c that is most likely attributed to underlying on- and off-axes magmatism (Fig. 2a, b). Also identifiable in the gravity anomaly profiles (Fig. 3b, d), this short-wavelength feature is not accounted for in our model. The thin plate deflections show much better fitting to the bathymetric profiles for 10-15 and 15-20 Ma. It is notable that the misfit between the 10-15 Ma profiles is only about 0.02.

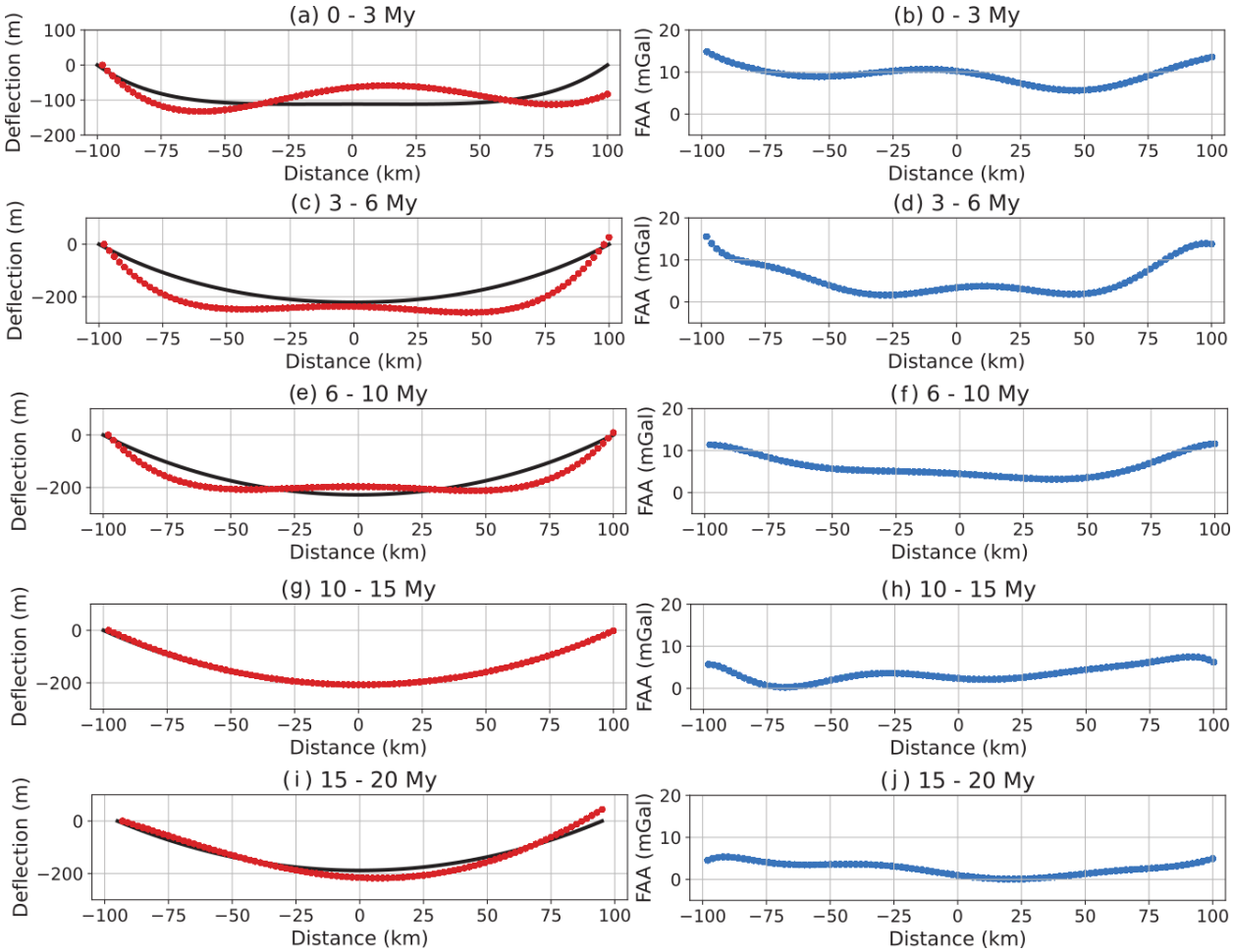

Figure 3. The best-fitting thin plate model's deflections (black, left column), the polynomial-fitted bathymetric profiles (red, left column), and the polynomial-fitted free-air gravity anomaly (ΔFAA) profiles (blue, right column) from the Chile Rise for (a, b) 0.1 - 3, (c, d) 3 - 6, (e, f) 6 - 10, (g, h) 10 - 15, and (i, j) 15 - 20 Ma. Note that the center of flowline has been shifted over time due to the curvature of the long-lived fracture zones. Each of the Chile Rise profiles are smoothed with filtering processes described in Section 2.1.

4. Discussion

The temporal evolution of the bathymetric profiles is characterized by the rapid initial deepening to about 200 m (Fig. 3a,c) and the profile reaches a more or less steady state after 6 Ma (Fig. 3e, g, i). This observation is seemingly ubiquitous in lithosphere segments bounded between fracture zones (Figure S2). Assessing this temporal evolution of lithosphere deflection provides an important insight on the validity of our model and guides us to future effort. The magnitude of the deflection observed in other fast-intermediate spreading lithosphere changes similarly with time (Figure S2), suggesting that the flexure is "frozen in" at the crustal age no older than 6 My where thermal gradient within lithosphere (e.g. 1250°C isotherm) becomes steepest to moderate (e.g., Audhkhasi & Singh, 2022). This steady state seen in the 10 Ma or older bathymetric profiles partially is also found in the temporal evolution of modeled deflection. The central deflection low reaches ~220 m in

subsequent 3-6 Ma time period after it reaches ~100 m, about half of the full deflection amount, in the 0-3Ma time period. Afterwards, the magnitude of the maximum deflection slightly decreases with time but stays around 200 m (6Ma ~) (Fig.4a). The brittle thickness of the lithosphere, $h(t)$, increases as the square root of time according to the half-space cooling model adopted in this study. The magnitude of bending moment and the flexural rigidity are proportional to $h^2(t)$ and $h^3(t)$ (Fig. 4b); and to t and $t^{3/2}$ (Fig. 4c). As a result, the M_e to D_e ratio decreases as $t^{-1/2}$ (Fig. 4d). As this ratio determines the deflection magnitude in our thin plate model, the deflection magnitude also decreases in time as seen in the periods after 6 Ma in our model.

One implication of the M_e to D_e ratio changing as $t^{-1/2}$ is that the ratio eventually approaches zero and thus the deflection magnitude also approaches zero although slowly. However, such behavior is not necessarily expected for the topographic expression in older lithosphere because the origin of the upward concave shape is the product of the balance between deviatoric thermal contraction and resistance to it, not bending moment as we assumed for convenience in this study.

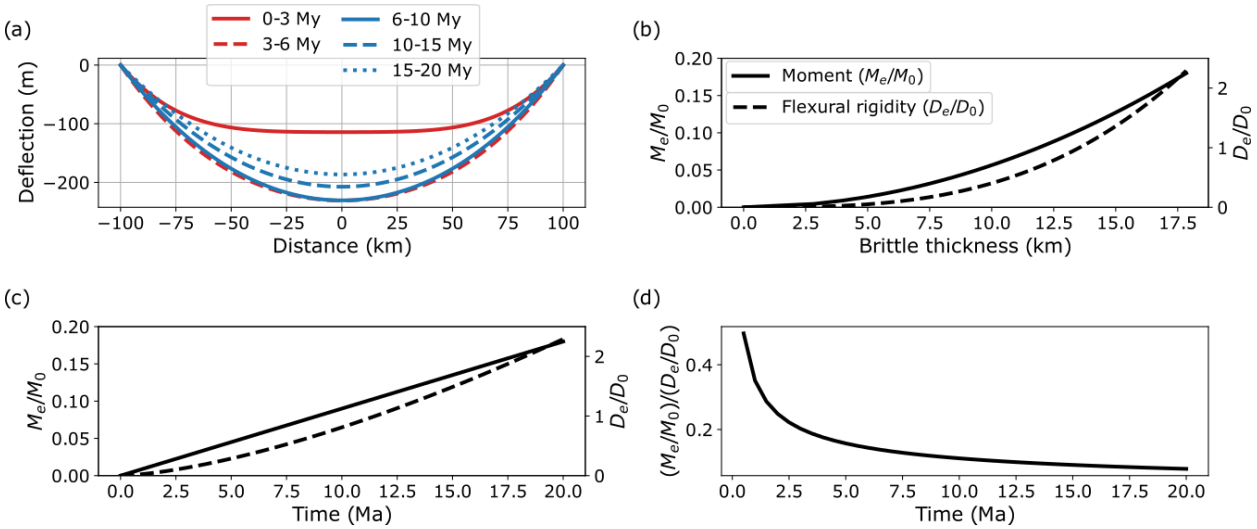

Figure 4. (a) Deflections of the model best fitting the Chile Rise bathymetry data averaged over five time periods, 0-3, 3-6, 6-10, 10-15, and 15-20 Ma. (b) Effective bending moment (M_e) and flexural rigidity (D_e) plotted as a function of brittle thickness ($h(t)$). M_e and D_e are normalized by the reference values (M_0 and D_0) for the brittle thickness at 10 Ma (h_0). (c) Normalized effective bending moment (M_e/M_0) and flexural rigidity (D_e/D_0) plotted as a function of time in Ma. (d) The ratio of the normalized effective bending moment to the normalized effective flexural rigidity plotted as a function of time (Ma).

The upward concavity in the gravity anomaly profiles corroborates the validity of our elastic flexure model. Since not isostatically compensated, the upward-concave flexure of an elastic plate by thermal contraction must produce free-air gravity anomaly of a self-similar pattern. When applied to the central low of ~200 m in the bathymetric profiles, the Bouguer plate correction formula, $2\pi G\Delta\rho\Delta h$, yields ΔFAA of about 15 mGal for $\Delta\rho$ equal to the density difference between basalt (2800 kg/m^3) and seawater (1030 kg/m^3) and Δh equal to 200 m. ΔFAA is about 10 mgal for 0-3 and 6-10 Ma (Fig. 3b, f) and about 15 mgal for 3-6 Ma (Fig. 3d). While the density structure needs to be better understood, these similar magnitudes of ΔFAA are consistent with our view that the 200-m amplitude of the upward concave bathymetric profiles is a product of thermal contraction of oceanic lithosphere as depicted in Fig. 1b.

The diminished magnitudes of ΔFAA for 10-20 Ma is apparently puzzling in the light of the deflection magnitude of 200 m maintained for these ages. However, it can be understood in terms of the upward continuation effects on the gravity anomaly profiles. The sea-level gravity anomaly profiles would be the upward continuation of those due to the uncompensated seafloor topography. The low-passing effect of upward continuation also reduces the overall amplitude, and the reduction magnitude is proportional to the seafloor depth. Because the seafloor depth increases with age, so does the amount of reduction in the gravity anomaly amplitude. Another possible explanation for the diminished gravity anomaly amplitudes would be geological processes such as the density-lowering alteration of oceanic crust due to hydrothermal circulation. The alteration near the fracture zone valleys is expected to be more extensive than in the middle of the lithospheric section. Accumulated over a sufficiently long time (i.e., > 10 Ma), the density-lowering alteration occurring more extensively near the fracture zones might counteract the gravity anomaly produced by the upward concave bathymetry.

The middle bulge seen in the Chile Rise bathymetry profiles for ages younger than 10 Ma (Fig. 3a, c, e) can be attributed to the combination of relatively thin crust over melt-rich region within relatively young, warm lithosphere, which is close to the spreading axis generating high isotherm gradient toward off axis (e.g., Cochran & Buck, 2001). Comparing with other lithosphere portions that are formed at fast to intermediate spreading rates, the curvature in young (0-3Ma) lithosphere can be unique to their underlying magmatism. The lithosphere curvature is clearly influenced by the nature and distribution of many off-axis seafloor products, including seamount chains and incipient rifts although magnitudes and upward concavity of the curvature seem to be very similar (Figs. S1 and S2).

5. Conclusions

The ridge-parallel bathymetric profiles from the 0-20 Ma fracture zones-bounded lithosphere formed at the Chile Rise have an upward concave shape of an amplitude of about 200 m. A thin elastic plate going through thermal contraction as illustrated in Fig. 1b can explain this observation. The free-air gravity anomaly is lower in the middle of the profiles for the Chile Rise lithosphere younger than 10 Ma by about 10-15 mgal. The magnitude is consistent with the Bouguer correction magnitude for the 200 m bathymetric low and the density difference between basalt and seawater. The consistency between the bathymetric and gravity anomaly profiles supports our view that oceanic lithosphere bounded by fracture zones can develop uncompensated upward concave flexure by thermal contraction.

A logical next step upon our study would be to construct a comprehensive thermomechanical numerical model to release the major simplifying assumptions made in this study and originally in PH86: e.g., the completely free shortening by mean thermal strain at all ages. This effort of refining currently widely accepted half-space cooling model and more accurately understanding crustal heat extraction via hydrothermal cooling (e.g., Kohli & Warren, 2020; Prigent et al., 2020), coupled with recent observations that highlights complicated thermal conditions within lithosphere (e.g., Audhkhasi & Singh, 2022), will advance our knowledge on thermal properties of lithosphere.

6. Open Research

All the data are obtained from publicly available bathymetry grid (Sandwell et al., 2014). Bathymetry profiles are extracted and plotted with GMT v.6 (e.g., Wessel et al., 2019). Open-source software SciPy (Virtanen et al., 2020) and matplotlib (Hunter, 2007) were used for calculating and plotting elastic flexures.

7. Supporting Information

Supporting Information is composed with two parts: Supplemental Information 1 containing Figures S1, S2, S3 and S4. Supplemental Information 2 containing Texts S1, S2, S3 and S4. Text S4 also includes links to Jupyter Notebooks (https://dx.doi.org/10.17605/OSF.IO/ZUK86) for reproducing Figures 3 and 4 and the associated data.

8. References

Audhkhasi, P., & Singh, S. C. (2022). Discovery of distinct lithosphere-asthenosphere boundary and the Gutenberg discontinuity in the Atlantic Ocean. *Science Advances*, *8*(24), eabn5404. https://doi.org/10.1126/sciadv.abn5404

Bonatti, E., Brunelli, D., Buck, W., Cipriani, A., Fabretti, P., Ferrante, V., et al. (2005). Flexural uplift of a lithospheric slab near the Vema transform (Central Atlantic): Timing and mechanisms. *Earth and Planetary Science Letters*, *240*(3–4), 642–655. https://doi.org/10.1016/j.epsl.2005.10.010

Buck, W. R. (2001). Accretional curvature of lithosphere at magmatic spreading centers and the flexural support of axial highs. *Journal of Geophysical Research: Solid Earth*, *106*(B3), 3953–3960. https://doi.org/10.1029/2000JB900360

Buck, W. Roger, Lavier, L. L., & Poliakov, A. N. B. (2005). Modes of faulting at mid-ocean ridges. *Nature*, *434*(7034), 719–723. https://doi.org/10.1038/nature03358

Cannat, M., Mamaloukas-Frangoulis, V., Auzende, J.-M., Bideau, D., Bonatti, E., Honnorez, J., et al. (1991). A geological cross-section of the Vema fracture zone transverse ridge, Atlantic Ocean; Ophiolites and the oceanic lithosphere. *Journal of Geodynamics*, *13*(2–4), 97–117.

Choi, E., & Gurnis, M. (2008). Thermally induced brittle deformation in oceanic lithosphere and the spacing of fracture zones. *Earth and Planetary Science Letters*, *269*(1), 259–270. https://doi.org/10.1016/j.epsl.2008.02.025

Cochran, J. R., & Buck, W. R. (2001). Near-axis subsidence rates, hydrothermal circulation, and thermal structure of mid-ocean ridge crests. *Journal of Geophysical Research: Solid Earth*, *106*(B9), 19233–19258. https://doi.org/10.1029/2001JB000379

Forsyth, D. W. (1979). Lithospheric flexure. *Reviews of Geophysics*, *17*(6), 1109–1114. https://doi.org/10.1029/RG017i006p01109

Gregory, E. P. M., Singh, S. C., Marjanović, M., & Wang, Z. (2021). Serpentinized peridotite versus thick mafic crust at the Romanche oceanic transform fault. *Geology*, *49*(9), 1132–1136. https://doi.org/10.1130/G49097.1

Grevemeyer, I., Rüpke, L. H., Morgan, J. P., Iyer, K., & Devey, C. W. (2021). Extensional tectonics and two-stage crustal accretion at oceanic transform faults. *Nature*, *591*(7850), 402–407. https://doi.org/10.1038/s41586-021-03278-9

Haxby, W. F., & Parmentier, E. M. (1988). Thermal contraction and the state of stress in the oceanic lithosphere. *J. Geophys. Res.*, *93*(6), 6419–6429.

Hunter, J. D. (2007). Matplotlib: A 2D graphics environment. *Computing in Science & Engineering*, *9*(3), 90–95. https://doi.org/10.1109/MCSE.2007.55

Juteau, T., Bideau, D., Dauteuil, O., Manac'h, G., Naidoo, D. D., Nehlig, P., et al. (1995). A submersible study in the western Blanco fracture Zone, N.E. Pacific: Structure and evolution during the last 1.6 Ma. *Marine Geophysical Researches*, *17*(5), 399–430. https://doi.org/10.1007/BF01371786

Kohli, A. H., & Warren, J. M. (2020). Evidence for a Deep Hydrologic Cycle on Oceanic Transform Faults. *Journal of Geophysical Research: Solid Earth*, *125*(2), e2019JB017751. https://doi.org/10.1029/2019JB017751

Kohli, A., Wolfson-Schwehr, M., Prigent, C., & Warren, J. M. (2021). Oceanic transform fault seismicity and slip mode influenced by seawater infiltration. *Nature Geoscience*, *14*(8), 606–611. https://doi.org/10.1038/s41561-021-00778-1

Kumar, R. R., & Gordon, R. G. (2009). Horizontal thermal contraction of oceanic lithosphere: The ultimate limit to the rigid plate approximation: HORIZONTAL CONTRACTION OF LITHOSPHERE. *Journal of Geophysical Research: Solid Earth*, *114*(B1). https://doi.org/10.1029/2007JB005473

Marjanović, M., Singh, S. C., Gregory, E. P. M., Grevemeyer, I., Growe, K., Wang, Z., et al. (2020). Seismic Crustal Structure and Morphotectonic Features Associated With the Chain Fracture Zone and Their Role in the Evolution of the Equatorial Atlantic Region. *Journal of Geophysical Research: Solid Earth*, *125*(10), e2020JB020275. https://doi.org/10.1029/2020JB020275

McNutt, M. K. (1984). Lithospheric flexure and thermal anomalies. *Journal of Geophysical Research: Solid Earth*, *89*(B13), 11180–11194. https://doi.org/10.1029/JB089iB13p11180

Mishra, J. K., & Gordon, R. G. (2016). The rigid-plate and shrinking-plate hypotheses: Implications for the azimuths of transform faults. *Tectonics*, *35*(8), 1827–1842. https://doi.org/10.1002/2015TC003968

Parmentier, E. M., & Haxby, W. F. (1986). Thermal stresses in the oceanic lithosphere: Evidence from geoid anomalies at fracture zones. *Journal of Geophysical Research: Solid Earth*, *91*(B7), 7193–7204. https://doi.org/10.1029/JB091iB07p07193

Prigent, C., Warren, J. M., Kohli, A. H., & Teyssier, C. (2020). Fracture-mediated deep seawater flow and mantle hydration on oceanic transform faults. *Earth and Planetary Science Letters*, *532*, 115988. https://doi.org/10.1016/j.epsl.2019.115988

Ren, Y., Geersen, J., & Grevemeyer, I. (2022). Impact of Spreading Rate and Age-Offset on Oceanic Transform Fault Morphology. *Geophysical Research Letters*, *49*(2), e2021GL096170. https://doi.org/10.1029/2021GL096170

Ryan, W. B. F., Carbotte, S. M., Coplan, J. O., O'Hara, S., Melkonian, A., Arko, R., et al. (2009). Global Multi-Resolution Topography synthesis. *Geochemistry, Geophysics, Geosystems*, *10*(3), Q03014. https://doi.org/10.1029/2008GC002332

Sandwell, D., & Fialko, Y. (2004). Warping and cracking of the Pacific plate by thermal contraction. *Journal of Geophysical Research: Solid Earth*, *109*(B10). https://doi.org/10.1029/2004JB003091

Sandwell, D., & Schubert, G. (1982). Lithospheric flexure at fracture zones. *Journal of Geophysical Research: Solid Earth*, *87*(B6), 4657–4667. https://doi.org/10.1029/JB087iB06p04657

Sandwell, D. T. (1986). Thermal stress and the spacings of transform faults. *Journal of Geophysical Research: Solid Earth*, *91*(B6), 6405–6417. https://doi.org/10.1029/JB091iB06p06405

Sandwell, D. T., Müller, R. D., Smith, W. H. F., Garcia, E., & Francis, R. (2014). New global marine gravity model from CryoSat-2 and Jason-1 reveals buried tectonic structure. *Science*, *346*(6205), 65–67. https://doi.org/10.1126/science.1258213

Tebbens, S. F., & Cande, S. C. (1997a). Southeast Pacific tectonic evolution from Early Oligocene to Present. *Journal of Geophysical Research: Solid Earth*, *102*(B6), 12061–12084. https://doi.org/10.1029/96JB02582

Tebbens, S. F., & Cande, S. C. (1997b). Southeast Pacific tectonic evolution from Early Oligocene to Present. *Journal of Geophysical Research: Solid Earth*, *102*(B6), 12061–12084. https://doi.org/10.1029/96JB02582

Turcotte, D. L., & Schubert, G. (2014). *Geodynamics* (3rd ed.). Cambridge University Press.

Virtanen, P., Gommers, R., Oliphant, T. E., Haberland, M., Reddy, T., Cournapeau, D., et al. (2020). SciPy 1.0: Fundamental Algorithms for Scientific Computing in Python. *Nature Methods*, *17*, 261–272. https://doi.org/10.1038/s41592-019-0686-2

Wang, Z., Singh, S. C., Prigent, C., Gregory, E. P. M., & Marjanović, M. (2022). Deep hydration and lithospheric thinning at oceanic transform plate boundaries. *Nature Geoscience*, *15*(9), 741–746. https://doi.org/10.1038/s41561-022-01003-3

Watts, A. B. (2001). *Isostasy and Flexure of the Lithosphere*. Cambridge University Press, Cambridge.

Wessel, P., Luis, J. F., Uieda, L., Scharroo, R., Wobbe, F., Smith, W. H. F., & Tian, D. (2019). The Generic Mapping Tools Version 6. *Geochemistry, Geophysics, Geosystems*, *20*(11), 5556–5564. https://doi.org/10.1029/2019GC008515

Wessel, Pål. (1992). Thermal stresses and the bimodal distribution of elastic thickness estimates of the oceanic lithosphere. *Journal of Geophysical Research: Solid Earth*, *97*(B10), 14177–14193. https://doi.org/10.1029/92JB01224

Wessel, Pål, & Haxby, W. F. (1990). Thermal stresses, differential subsidence, and flexure at oceanic fracture zones. *Journal of Geophysical Research: Solid Earth*, *95*(B1), 375–391. https://doi.org/10.1029/JB095iB01p00375

Wilson, J. T. (1965). A new class of faults and their bearing on continental drift. *Nature*, *207*(4995), 343–347.

Geophysical Research Letters

Supporting Information for

A thin elastic plate model for thermally contracting young oceanic lithosphere: Insights from comparison with modern seafloor observations

Eunseo Choi[1] and Masako Tominaga[2]

1. Center for Earthquake Research and Information, the University of Memphis and 2: Woods Hole Oceanographic Institution

Contents of this file

Text S1 on the smoothing of bathymetry and gravity anomaly profiles

Test S2 on the sediment thickness in the Chile Rise region

Text S3 on the adjusting factors for bending moment and flexural rigidity

Text S4 on the numerical method used for the elastic flexure calculation

Text S1 Smoothing applied to the profiles of bathymetry and gravity anomaly

The raw profiles acquired from ETOPO1 as described in Sec. 2.1 of the main text are smoothed before fitted to a polynomial to remove short-wavelength signals from seamounts, seamount chains, intraplate magmatic overprints, etc., that are geologically obvious in the plane-view bathymetry grids. The applied smoothing operation is the convolution with a symmetric, normalized, linear kernel of a window size of 9. Because of the symmetry with respect to the central point of the kernel and the linearity, the convolution is equivalent to weighted averaging within a data point-centered window with nine weights (2, 3, 4, 5, 6 ,5, 4, 3, 2), each of which is normalized by 34. As intended with the chosen kernel size, the effects of the applied smoothing effects are noticeable only in the small-wavelength components (Fig. ST1.1). The results presented in the main text are insensitive to window sizes: Mid- to long-wavelength features, essential for determining the concavity of the profiles, are retained in both gravity profiles with the window size 9 (Fig. ST1.2) and 23 (Fig. ST1.3).

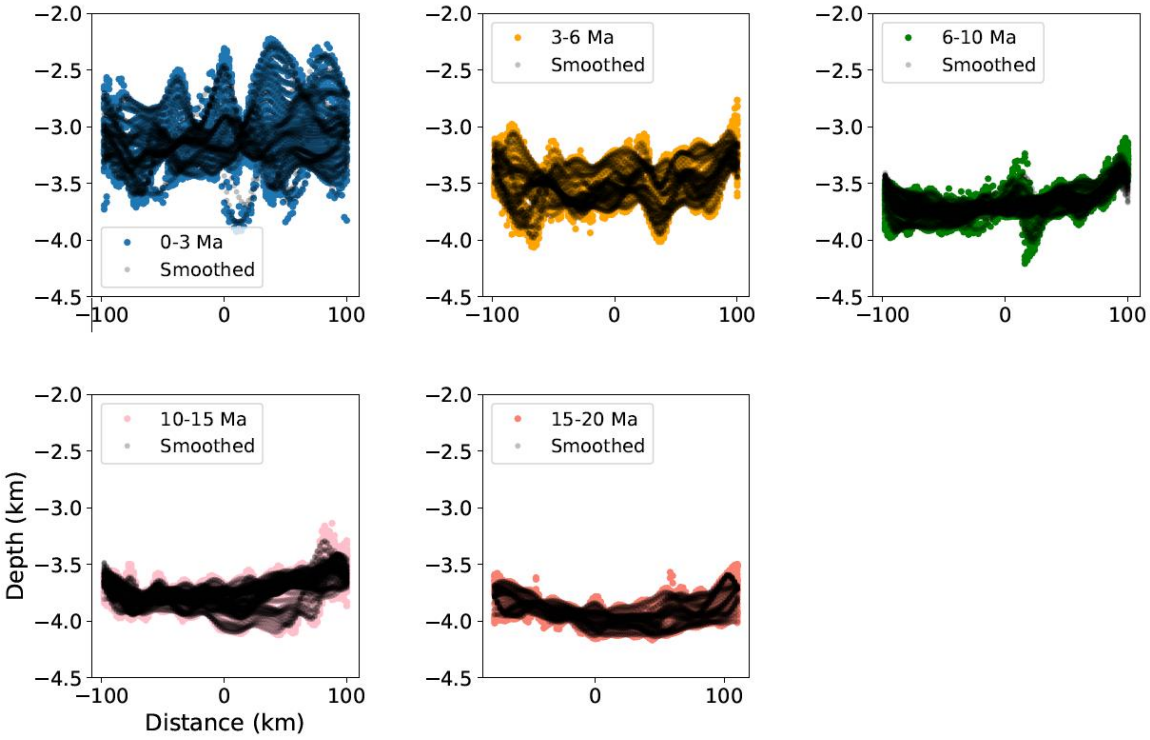

Figure ST1.1: Raw and smoothed bathymetry profiles for the Chile Rise region.

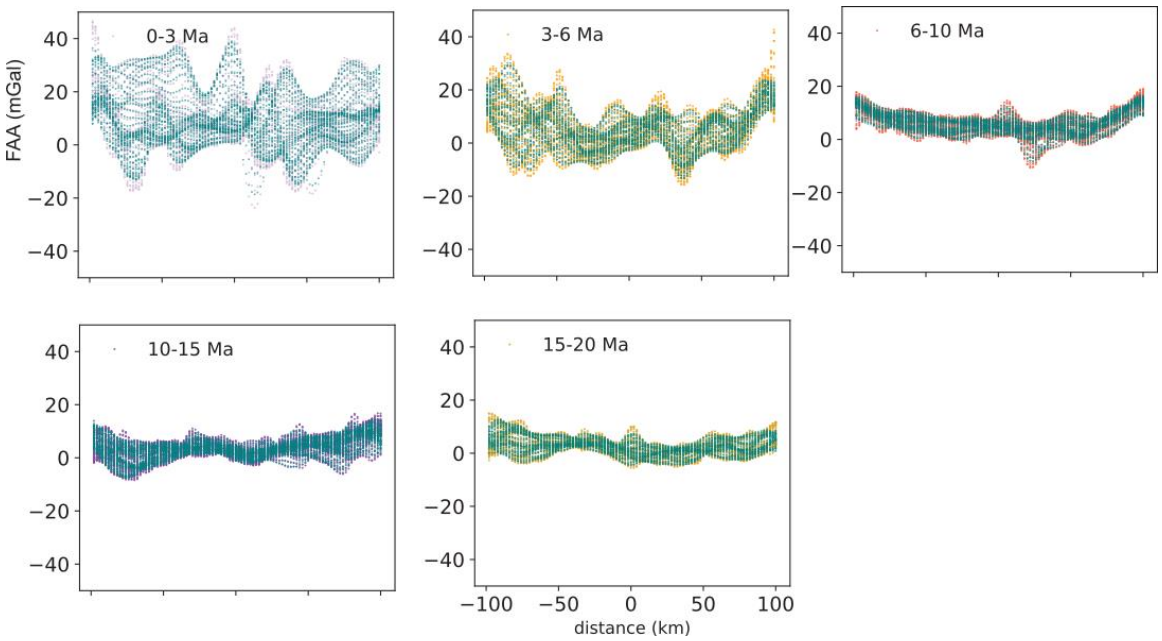

Figure ST1.2: Raw and smoothed (teal) gravity profiles for the Chile Rise region. The smoothing window size was 9.

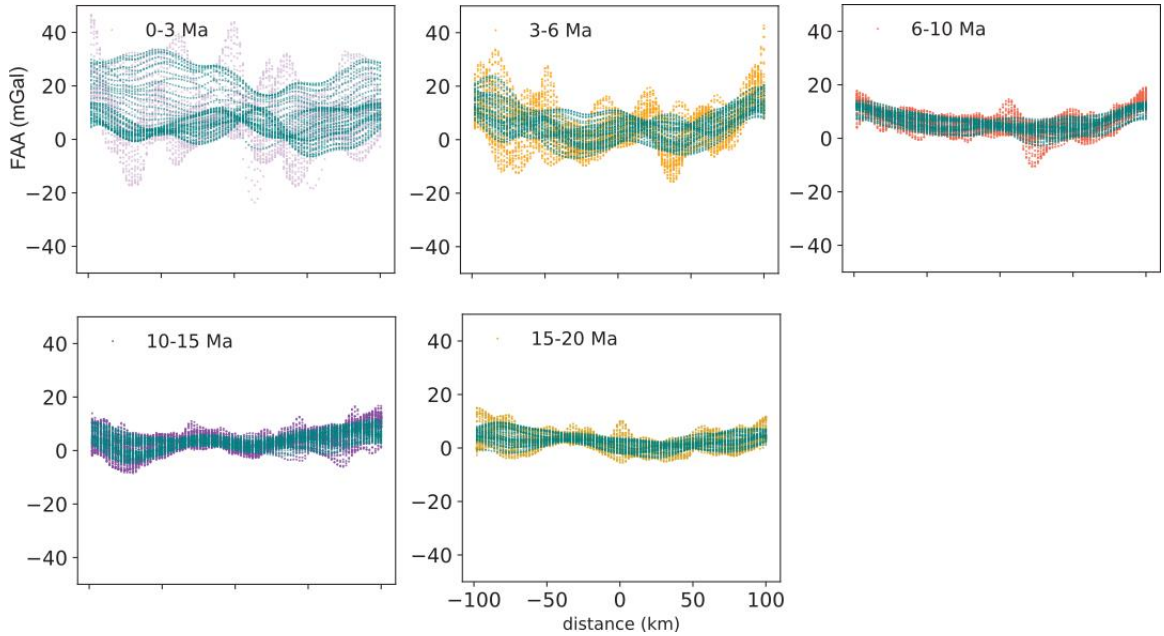

Figure ST1.3: Same as Fig. ST1.2 but the window size was 23.

Text S2. Sediment thickness in the Chile Rise region

The vintage chirp sonar imagery, one of the most direct pieces of information on seafloor sediment thickness, shows that the sediment layer in the case study area is only a few tens of meters thick (Fig. ST2). GlobSed, a global total sediment thickness data set (Straume et al., 2019) consistently shows that the 0-20 Ma ocean floor formed west of the Chile Rise has less than 100 m-thick sediments and the thickness variations are even smaller, 20-30 m, both along and across the plate spreading direction. Furthermore, GlobSed shows that sediment thickness variations along our profiles are semi-linear. If they have any effect, most of them must be effectively removed together with the linear trend that we remove from the bathymetric and gravity anomaly profiles.

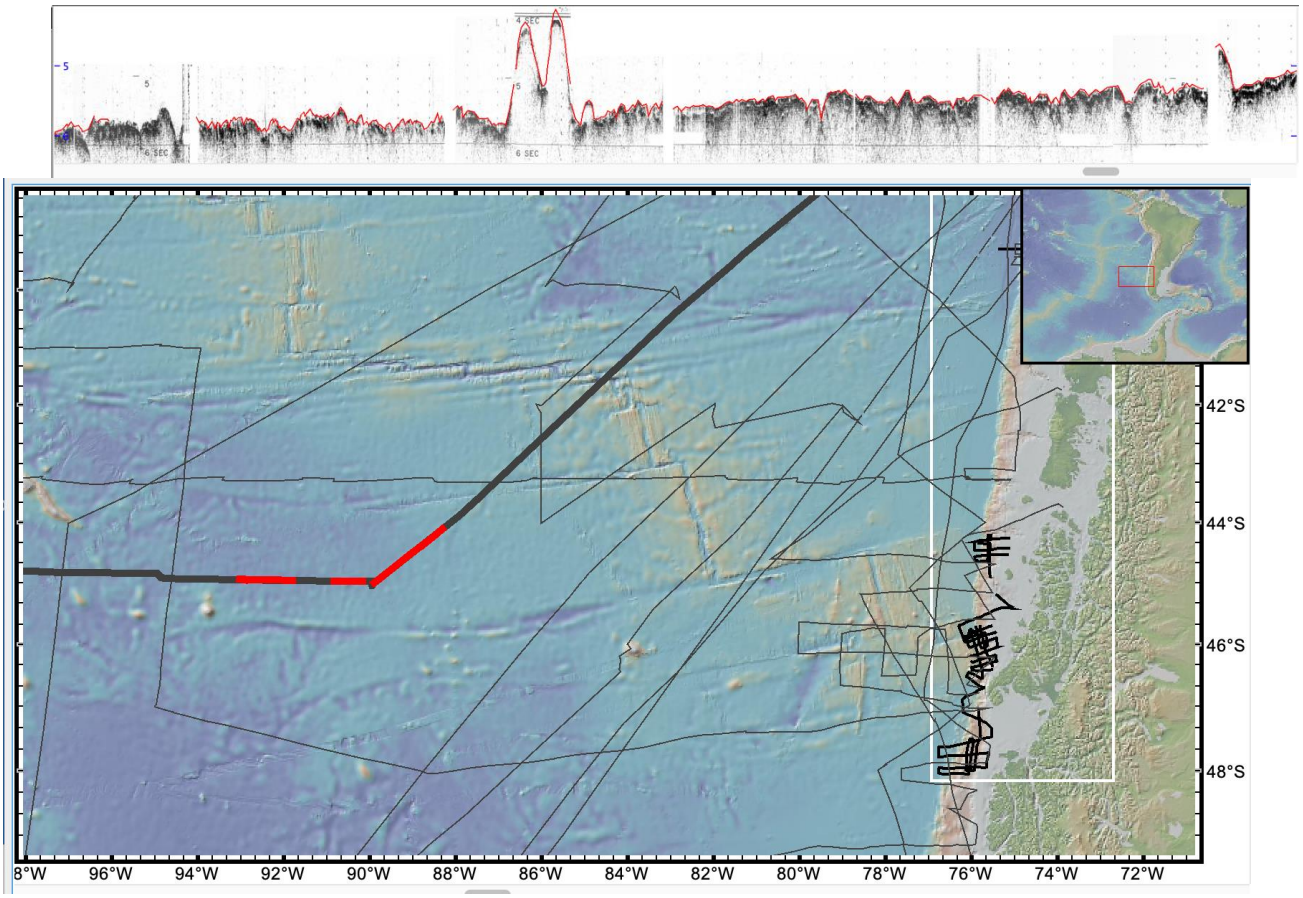

Figure ST2: An example of available analogue seismic reflection record (top) from the spreading corridor of Chile Rise (bottom) where we have used cross-lithosphere profiles. Cruise ID: ELT20.

Text S3 Effective bending moment and flexural rigidity

The bending moment computed by eq. (5) in the main text is an overestimation because the deviatoric thermal contraction must not occur freely in oceanic lithosphere. We can only estimate the true proportion of the deviatoric thermal strain that occurs causing bending. The approach we take here is to introduce effective bending moment and flexural rigidity, $M_e(t)$ and $D_e(t)$. For simplicity, $M_e(t)$ and $D_e(t)$ are defined as $M_{\text{adj}}M(t)$ and $D_{\text{adj}}D(t)$. We define the best-fitting M_{adj} and D_{adj} as those minimizing the misfit,

$$e\left(M_{\text{adj}},\, D_{\text{adj}}\right) = \sum_{i=1}^{5} \frac{\left\| w_i\left(\boldsymbol{x};\, M_{\text{adj}},\, D_{\text{adj}}\right) - w_i^{\text{obs}}(\mathbf{x}) \right\|}{\left\| w_i^{\text{obs}}(\mathbf{x}) \right\|},$$

where $\|\cdot\|$ is the L_2 norm, the index i corresponds to the five time periods, 0-3, 3-6, 6-10, 10-15, and 15-20 Ma, and $\boldsymbol{x}$ is the common locations for both profiles. Noting the irregularities visible in the young-age profiles, we also compute the misfits as the partial sum for i = 4 and 5 only. The total and partial misfits for M_{adj} between 0 and 0.8 and D_{adj} in the range of 0 to 10 are shown in Fig. TS1a and b, respectively. The best-fitting values based on the total misfit ("Best") are 0.1 and 1.0 (Fig. ST3a). The partial misfits do not show a well-defined minimum but are generally low for any pair of M_{adj} and D_{adj} when their ratio is about 0.1 (Fig. ST3b). The best-fitting values based on the partial misfits ("Best_ps") are 0.22 and 2.2; and the corresponding thin plate deflections are shown and compared with the filtered and polynomial-fitted bathymetric profiles from the Chile Rise in Fig. ST4.

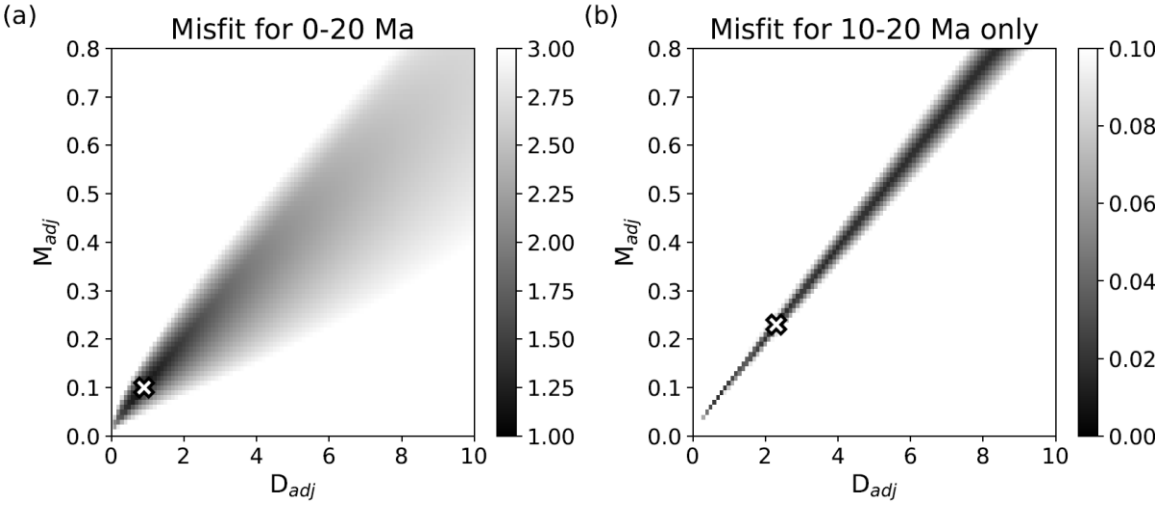

Figure ST3: (a) Total misfits between the bathymetric profiles and our modeled deflection profiles for $0 \leq M_{\text{adj}} \leq 0.8$ and $0 \leq D_{\text{adj}} \leq 10$. (b) Same as (a) except that partial misfits are shown.

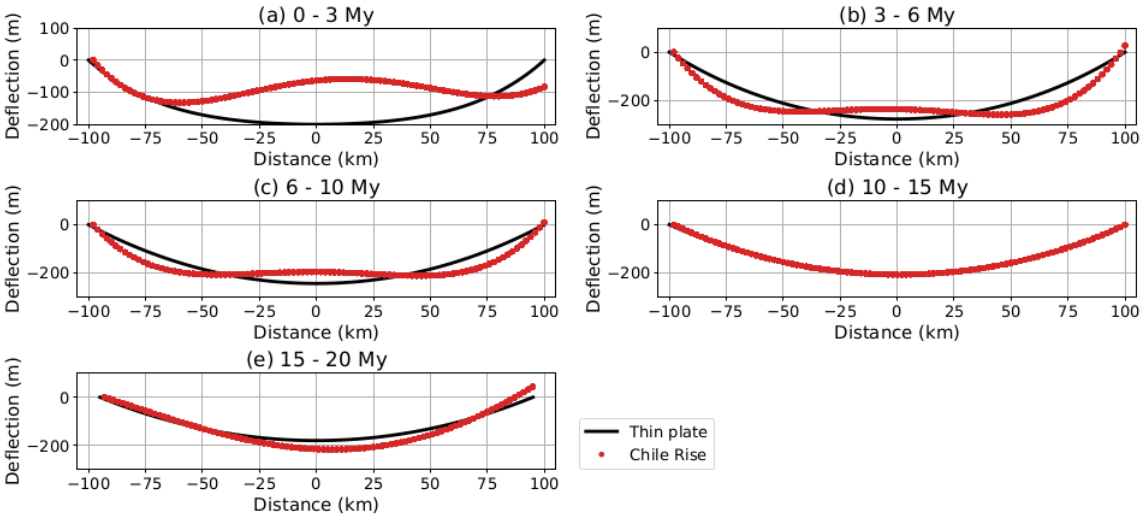

Figure ST4: Deflections (black) of the best-fitting thin plate model based on the partial misfit ($\boldsymbol{M}_{adj}$ = 0.22 and $\boldsymbol{D}_{adj}$ = 2.2) and the polynomial-fitted bathymetric profiles from the Chile Rise (red) for (a) 0.1 - 3, (b) 3 - 6, (c) 6 - 10, (d) 10 - 15, and (e) 15 - 20 Ma.

The 0-3 My profile from the Best_ps ("partial misfits", see the ST3) model (Fig. ST4a) well coincides with the bathymetric profiles over about 30 km from the left end in Fig. ST4a. The Best model's profile for the corresponding period is less steep near the ends (Fig. 3a in the main text). However, because of the middle bulge, the misfit for this time period is much greater in the Best_ps model than in the Best one (Table ST1). For 3-6 and 6-10 My, the near-end slopes of the Best_ps model are steeper than those of the Best model (Fig. ST4b, c; cf. Fig. 3c, e) but do not as well coincide with the bathymetric profiles as in the period of 0-3 My. The degree of misfits within the Best_ps model are comparable to those of the Best model in these time periods (Table ST1). The profiles for the later time periods well coincide with the those from the Best model and also with the bathymetric profiles (Fig. ST4d, e; Fig. 3g, i). Both models' misfits for the periods, 10-15 and 15-20 My, are similar (Table ST1).

Table ST1: Misfits per time period

	0-3 My	3-6 My	6-10 My	10-15 My	15-20 My	Sum or Partial Sum
Best	0.392	0.283	0.200	0.021	0.278	1.174
Best_ps	0.897	0.196	0.202	0.017	0.285	1.597

Text S4. The method for the elastic flexure calculation

With no horizontal force and the isostatic restoring force, the one-dimensional bending equation for a thin elastic plate (Turcotte & Schubert, 2014, TS14 hereafter) becomes

$$w(x)'''' + \frac{(\rho_m - \rho_w)g}{D(t)} w(x) = 0,$$

where $w(x)$ is the vertical deflection, ρ_m and ρ_w are mantle and water densities, g is the gravitational acceleration, and $D(t)$is the flexural rigidity defined as $Eh(t)^{3/}\big(12(1-\nu^2)\big)$ with $h(t)$ being the brittle thickenss corresponding to 500°C at a given time, t. Since we are interested in the relatively young age range, 0 to 20 Ma, $h(t)$ are approximated as those of the half-space cooling model (TS14). With the surface (T_0) and mantle temperature (T_1) of 0°C and 1300°C and the brittle-ductile transition temperature (T_l) of 500°C, the half-space cooling model provides the following relationship:

$$\frac{T_l - T_0}{T_1 - T_0} = \frac{500}{1300} \approx 0.3846 = \mathrm{erf}\Big(h/\big(2\sqrt{\kappa t}\big)\Big).$$

Solving for h, we get

$$h(t) = 0.7104\sqrt{\kappa t}.$$

For other values of T_l,

$$h(t) = 2\mathrm{erf}^{-1}(T_l\,/1300)\sqrt{\kappa t}.$$

We choose the following representative values for the parameter appearing in the expressions given above: ρ_m is 3300 kg/m^3, ρ_w is 1030 kg/m^3, α_v is $3\alpha_l$ with $\alpha_l = 1.0 \times 10^{-5}$ K^{-1}, and κ is 10^{-6} m^2/s.

The boundary conditions are $w(0) = 0$, $w''(0) = M/D$, $w''(L) = 0$, and $w''(L) = M/D$. where M is the bending moments of which definition is given in the main text.

The horizontal distance variable, x, and vertical deflection, w, are non-dimensionalized to $\overline{x}$ and $\overline{w}$ as

$$x = \alpha_0\,\overline{x} \text{ and} w = \frac{D_0}{M_0}\overline{w},$$

where $\alpha_0 = \left[\frac{D_0}{(\rho_m - \rho_w)g}\right]^{\frac{1}{4}}$, $D_0 = \frac{Eh_0^3}{12(1-\nu^2)}$, and $M_0 = \frac{1}{12}\alpha E' T_l h_0^2$. h_0Is the brittle thickness corresponding to T_l of 500 °C and the age of 10 Ma.

These scaling leads to the following relationships between the derivatives of w and $\overline{w}$:

$$w(x) = \frac{D_0}{M_0}\overline{w}(\alpha_0\overline{x}),$$

$$w'(x) = \frac{D_0}{M_0}\frac{d\overline{w}}{d\overline{x}}\frac{d\overline{x}}{dx} = \frac{D_0}{M_0\alpha_0}\overline{w}',$$

$$w''(x) = \frac{D_0}{M_0\alpha_0^2}\overline{w}'',$$
$$w'''(x) = \frac{D_0}{M_0\alpha_0^3}\overline{w}''', \text{ and}$$
$$w''''(x) = \frac{D_0}{M_0\alpha_0^4}\overline{w}''''.$$

Using the above relations, we carry out the non-dimensionalization of the original equation as follows:

$$w'''' + \frac{(\rho_m - \rho_w)g}{D}w = 0$$
$$\Rightarrow \frac{D_0}{M_0\alpha_0^4}\overline{w}'''' + \frac{(\rho_m - \rho_w)g}{D}\frac{D_0}{M_0}\overline{w} = 0$$
$$\Rightarrow \overline{w}'''' + \frac{D_0}{D}\overline{w} = 0.$$

The boundary conditions for the non-dimensional equation are $\overline{w}(0) = 0$, and $w''(0) = \frac{M}{D}$,

$$\Rightarrow \frac{D_0}{M_0\alpha_0^2}\overline{w}''(0) = \frac{M}{D}$$
$$\Rightarrow \overline{w}''(0) = \frac{M}{D}\frac{M_0\alpha_0^2}{D_0}$$

on the left ($\overline{x} = 0$) boundary; $\overline{w}(L/\alpha_0) = 0$ and

$$\overline{w}''(L/\alpha_0) = \frac{M}{D}\frac{M_0\alpha_0^2}{D_0}$$

on the right boundary ($\overline{x} = L/\alpha_0$).

The reference values for nondimensionalization, D_0 and α_0, do not necessarily coincide with the coefficients of the flexure equation, D and α because D and α are time-dependent through the brittle thickness, $h(t)$.

To acquire an approximate solution to the above non-dimensionalized forth-order ordinary differential equation (ODE) and the associated boundary conditions, we follow the standard solution procedure for high-order ODEs, which is to convert a high-order ODE to a system of 1st order ODEs as follows:

$$\overline{w}_0 = \overline{w},$$
$$\overline{w}_0'\left(= \overline{w}'\right) = \overline{w}_1,$$
$$\overline{w}_1'\left(= \overline{w}''\right) = \overline{w}_2,$$
$$\overline{w}_2'\left(= \overline{w}'''\right) = \overline{w}_3,$$
$$\overline{w}_3'\left(= \overline{w}''''\right) = -\frac{D_0}{D}\overline{w}_0.$$

This system of 1st order ODEs can be numerically integrated. We use SciPy's `solve_bvp` module.

The presented solution procedure is implemented in a Jupyter notebook available at https://dx.doi.org/10.17605/OSF.IO/ZUK86 (Files -> "ipynb and input files for elastic flexure modeling" directory -> "solving plate equation with moment.ipynb").

References

Straume, E. O., Gaina, C., Medvedev, S., Hochmuth, K., Gohl, K., Whittaker, J. M., et al. (2019). GlobSed: Updated Total Sediment Thickness in the World's Oceans. *Geochemistry, Geophysics, Geosystems*, *20*(4), 1756–1772. https://doi.org/10.1029/2018GC008115

Turcotte, D. L., & Schubert, G. (2014). *Geodynamics* (3rd ed.). Cambridge University Press.

Geophysical Research Letters

Supporting Information for

A thin elastic plate model for thermally contracting young oceanic lithosphere: Insights from comparison with modern seafloor observations

Eunseo Choi[1] and Masako Tominaga[2]

1. Center for Earthquake Research and Information, the University of Memphis and 2: Woods Hole Oceanographic Institution

Contents of this file

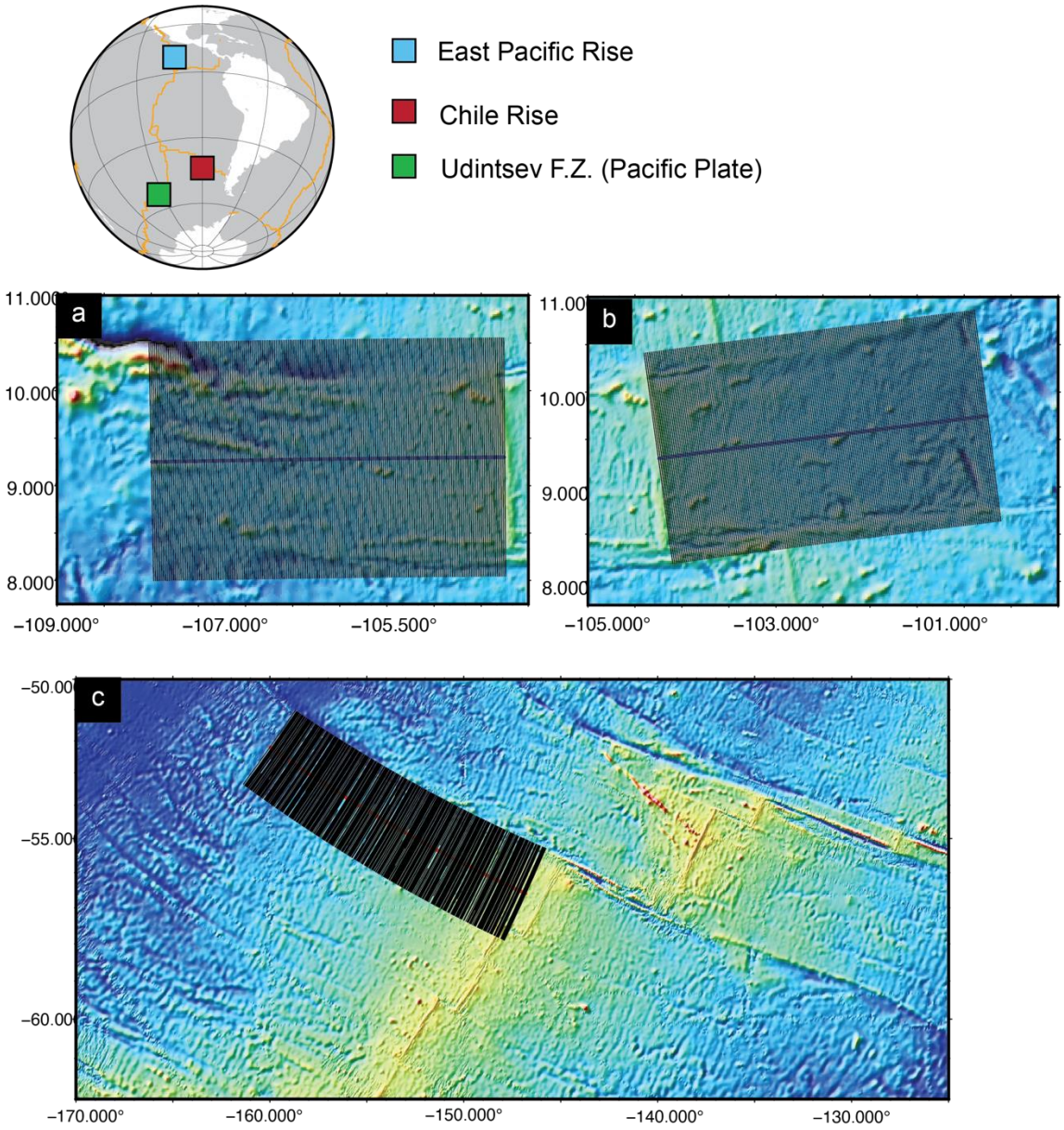

Figure S1: Examples of how bathymetry profiles are extracted from ETOPO1-arc minute compilation initially. Map and each panel showing the locations of intermadiate spreading Chile Rise (main text), (a) fast-spreading western/Pacific plate side of the East Pacific Rise 9° N lithosphere; (b) fast-spreading eastern/Cocos plate side of the EPR 9° N lithosphere; and (c) intermediate spreading lithosphere at Udintsev fracture zone. Thin black solid lines show the collections of ridge-parallel data profiles (see Method §2.1).

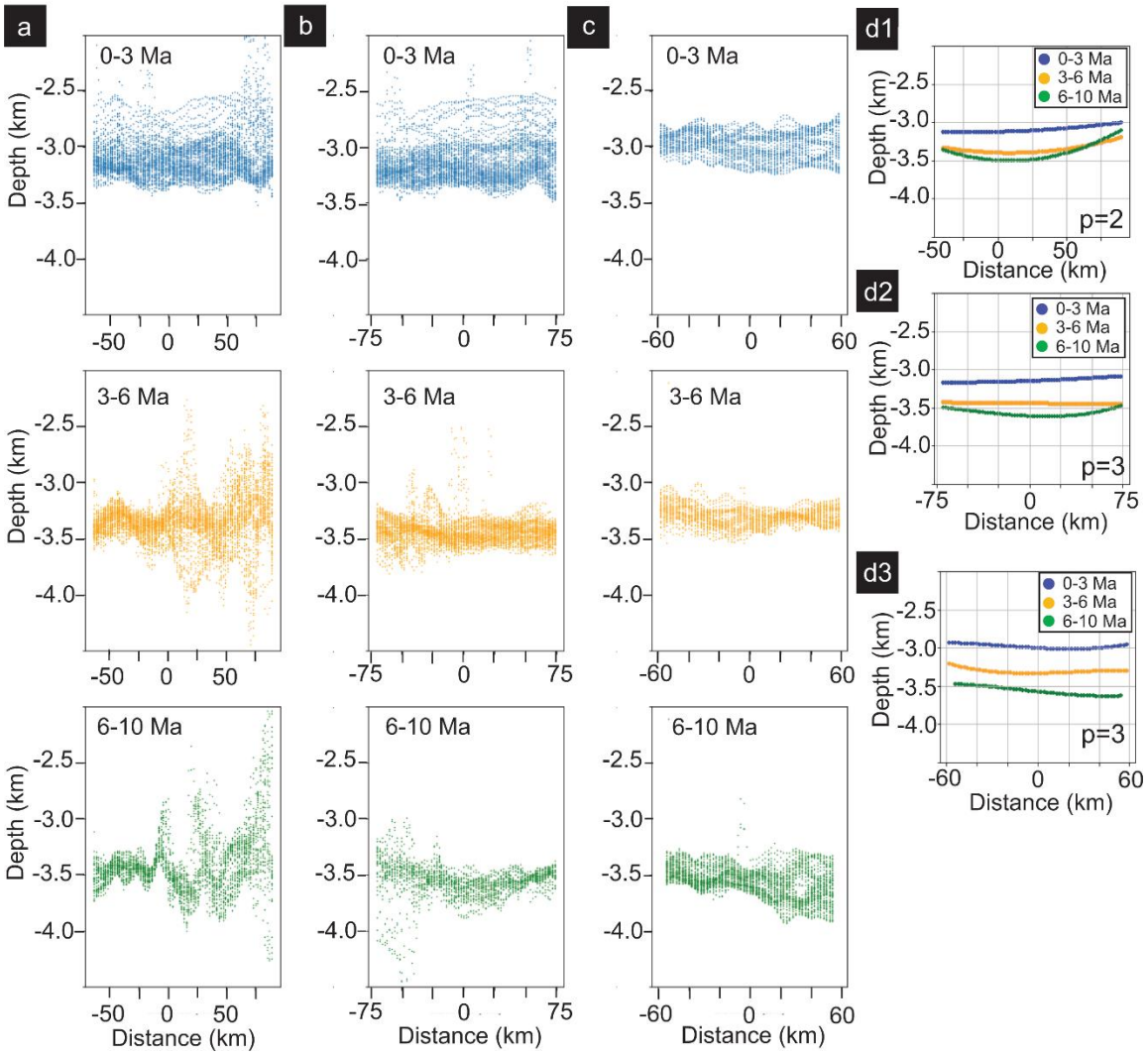

Figure S2: Bathymetry profiles extracted from (a) fast-spreading western/Pacific plate side of the East Pacific Rise 9° N lithosphere; (b) fast-spreading eastern/Cocos plate side of the EPR 9° N lithosphere; and (c) intermediate spreading lithosphere at Udintsev Fracture Zone. Data point showing depth data sampled at every 2km along the ridge-parallel profiles are collected at 2km increment along age flow-line. Panels are divided into three time periods to show their curvature characteristics (see the main text §2.1 and §3.1). Due to the ambiguity of the fracture zone locations and flow line curvature, we only show here the crustal age up to 10 Ma. We then applied low-pass filter to eliminate extremes and obvious outliers from each profile line and conducted polynomial curve fitting to examine the first-order curvature of lithosphere in each time period for: (d1) fast-spreading western/Pacific plate side of the East Pacific Rise 9° N lithosphere; (d2) fast-spreading eastern/Cocos plate side of the EPR 9° N lithosphere; and (d3) intermediate spreading lithosphere at Udintsev Fracture Zone.

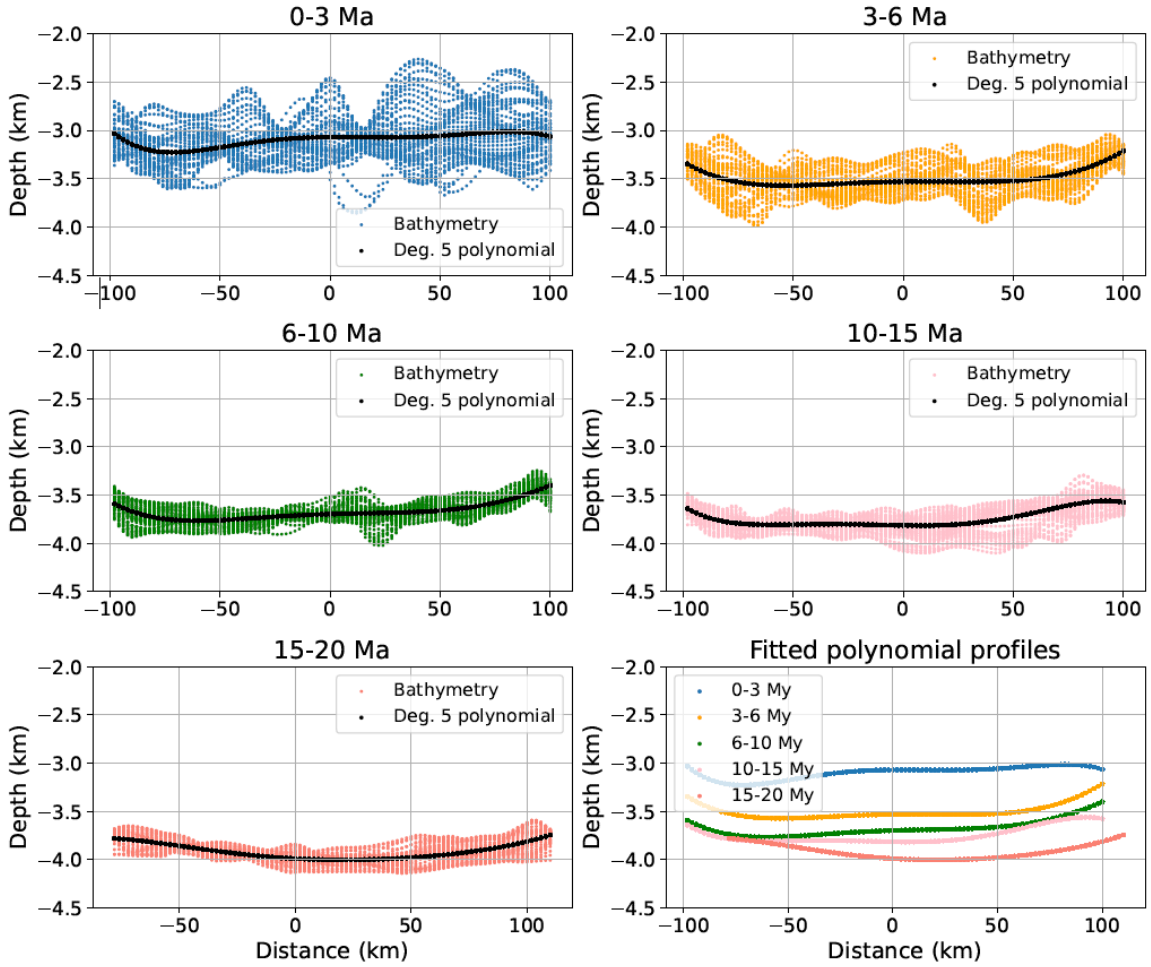

Figure S3: Smoothed bathymetry profiles for the Chile Rise and the result of the polynomial fitting to each of the time intervals.

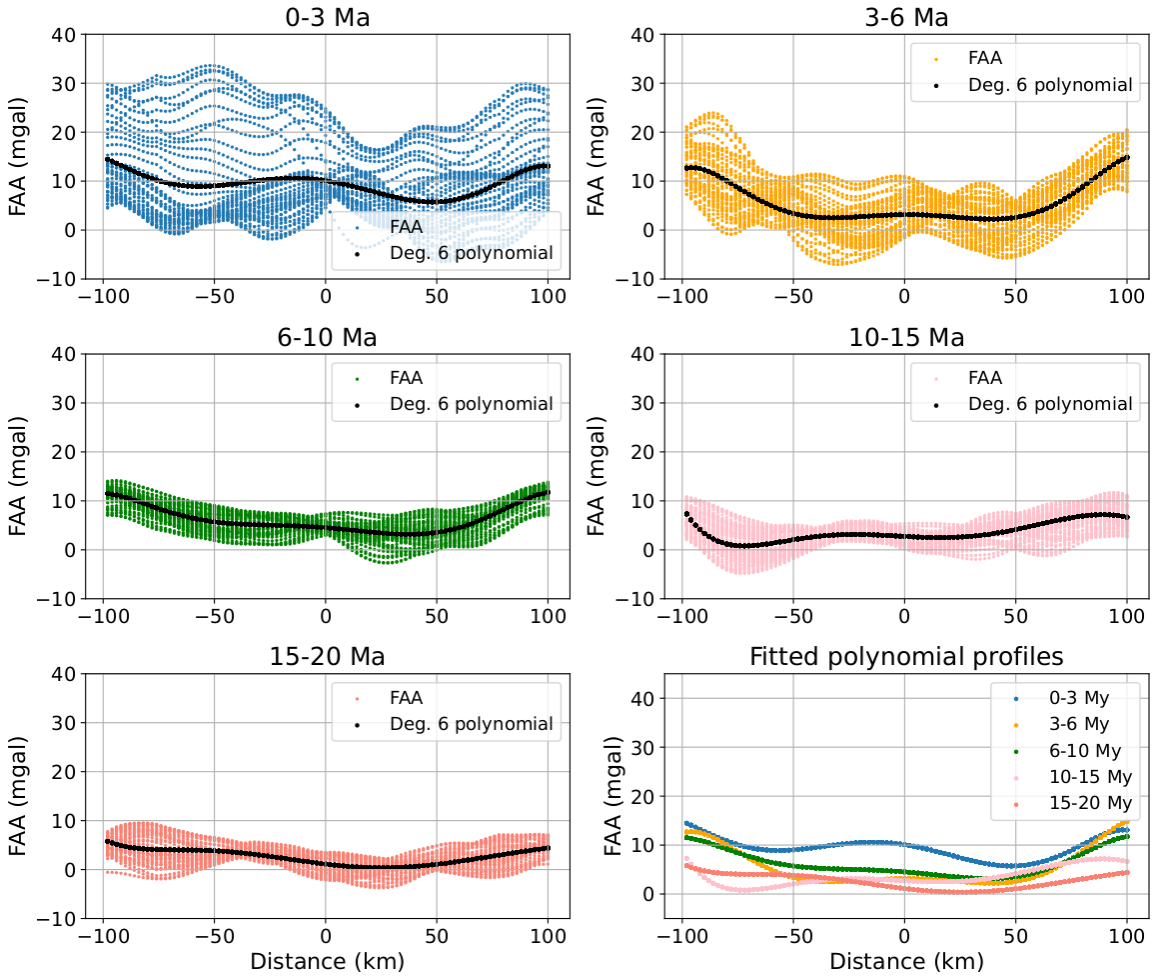

Figure S4: Smoothed free-air gravity anomaly profiles for the Chile Rise and the result of the polynomial fitting to each of the time intervals.